Compact dynamical model of brain activity

J. W. Kim[1,2] and P. A. Robinson[1,2,3]
[1]*School of Physics, The University of Sydney, Sydney, New South Wales 2006, Australia*
[2]*Brain Dynamics Center, Westmead Millennium Institute, Westmead Hospital and Western Clinical School of The University of Sydney, Westmead, New South Wales 2145, Australia*
[3]*Faculty of Medicine, The University of Sydney, Sydney, New South Wales 2006, Australia*
(Received 13 September 2006; revised manuscript received 17 December 2006; published 8 March 2007)

A compact physiologically based mean-field formulation of brain dynamics is proposed to model observed brain activity and electroencephalographic (EEG) signals. In contrast to existing formulations, which are more detailed and complicated, our model is described by a single second-order delay differential equation that encapsulates salient aspects of the physiology. The model captures essential features of activity mediated by fast corticocortical connections and delayed feedbacks via extracortical pathways and external stimuli. In the linear regime, these features can be simply expressed by three coefficients derived from the properties of these physiological pathways and explicit nonlinear approximations are also derived. This compact model successfully reproduces the main features of experimental EEG's and the predictions of previous models, including resonance peaks in EEG spectra and nonlinear dynamics. As an illustration, key features of the dynamics of epileptic seizures are shown to be reproduced by the model. Due to its compact form, the model will facilitate insight into nonlinear brain dynamics via standard nonlinear techniques and will guide analysis and investigation of more complex models. It is thus a useful tool for analyzing complex brain activity, especially when it exhibits low-dimensional dynamics.

DOI: 10.1103/PhysRevE.75.031907 PACS number(s): 87.10.+e, 87.19.−j, 87.18.−h

I. INTRODUCTION

The complex dynamics of brain function has been an active topic of interest for decades [1–3]. In particular, electroencephalograms (EEG's) resulting from cortical electrical activity have been widely used as a tool in neuroscience and medicine. As an approach to integrating various properties of EEG's, mean-field continuum models of brain dynamics have been developed since the 1970s [4–12]. Within this class of models, various authors have incorporated realistic anatomical and physiological features such as excitatory and inhibitory neural populations, nonlinear neural threshold firing responses, dendritic, cell-body and axonal dynamics, and corticothalamic feedback (detailed overviews are available in Refs. [13–16] and references therein). Recent work in this area has reported a number of quantitatively verified predictions of EEG's, such as spectral peaks corresponding to different brain states [17,18], evoked response potentials (ERP's) [19], generalized epileptic seizures [17,20], and measures of coherence [21].

Despite their many successes, previous continuum models are difficult to explore systematically because they involve relatively large numbers of quite complicated equations with many parameters. For example, the model in Ref. [22] has a set of four second-order delay differential equations with 10–15 physiologically constrained parameters, depending on the variant. Although some properties of EEG's, such as spectral peaks, can be well understood by linear instability analysis of the model, nonlinear behaviors are hard to explore analytically. There are some specific cases where certain nonlinear properties, such as limit cycles and chaotic attractors, are observed. For example, Le Van Quyen *et al.* [23] demonstrated that saddle-node behavior is embedded in low-dimensional chaotic brain dynamics by analyzing EEG's during epileptic seizures. In addition, the onsets of instability of a brain at resonance frequencies can be parametrized in a reduced space [17]. Stable limit cycles emerge when the brain passes the instability boundaries, as was recently verified by a mean-field approach [17,20]. These results show that the brain exhibits low-dimensional dynamics under some conditions and such dynamics can thus potentially be described by a simpler model with fewer equations and parameters than has hitherto been achieved.

Motivated by the above points, our first aim is to obtain a simple model for cortical dynamics by adapting and approximating the aforementioned continuum model [12,15,22]. The compact model describes the brain using a single second-order delay differential equation which has only one explicit variable: the corticocortical excitatory activity. The second aim of the paper is to verify that the compact model retains the key dynamical features of the more general one. In doing this, we show that the model can be linearized near steady states, keeping the essential features such as corticocortical propagation and delayed feedbacks via simplified extracortical pathways and external stimuli; in addition, a cubic nonlinear approximation is derived near fixed points. These features can then be simply expressed by three coefficients derived from the properties of these physiological pathways. When driven by white noise, representing external stimuli, we verify that our model reproduces and unifies many linear and nonlinear properties of EEG's, such as spectral peaks and epileptic seizure dynamics, in a physiologically plausible parameter region, thereby combining many successes of recent modeling with greater simplicity and insight.

The relevant aspects of the previous corticothalamic model are briefly outlined in Sec. II. A compact model is derived based on the relevant physiology (the central outcome of the paper) and related to the previous corticothalamic model in Sec. III A. We then verify that the compact

model has similar dynamical properties to more complex ones. Section III B studies basic properties of the model, such as steady-state behavior, spectral properties, and linear instabilities, and verifies that they preserve the essential features of more complex analyses, including the electrophysiologically well-known EEG spectral peaks of the slow-wave ($\lesssim$1 Hz), α ($\sim$10 Hz), and θ ($\sim$4 Hz) bands. The stability zone in parameter space is then discussed and compared with previous model approaches, and we show that limit-cycle solutions can exist under certain conditions. Furthermore, a linearized model and a simplified nonlinear model are derived from the compact model in the vicinity of steady states, and their properties are investigated in Secs. III C and III D, respectively. As an additional concrete illustration and verification of the model, seizure frequencies, onsets, and dynamics are examined in Sec. IV. This work lays the foundation for use of the model in analyzing other phenomena and as a guide to analysis and investigation of more complicated models, somewhat akin to the role of simplified single-neuron models (e.g., leaky integrate and fire) in assisting analysis of conductance-based (e.g., Hodgkin-Huxley) formulations of neuronal dynamics.

II. CORTICOTHALAMIC MODEL

We consider a continuum brain model developed by Robinson *et al.* [12,15,22], from which a more compact model is derived in Sec. III. Since the details of the model can be found in the literature, we restrict ourselves here to a brief outline.

The first feature incorporated is the neural response to the cell-body potential. Mean firing rates Q_a of excitatory ($a=e$) and inhibitory ($a=i$) neurons are nonlinearly related to mean potentials V_a, measured relative to the resting level, by $Q_a(\mathbf{r},t)=S[V_a(\mathbf{r},t)]$, where S is a sigmoidal function that increases from 0 to $Q_{\max}$ as V_a increases from $-\infty$ to $+\infty$. We use

$$Q_a = S(V_a) = \frac{Q_{\max}}{1+e^{-(V_a-\theta)/\sigma'}}, \tag{1}$$

where θ is the mean firing threshold and $\sigma'\pi/\sqrt{3}$ is its standard deviation.

The potential V_a results after dendritic inputs have been filtered and smeared out in time while passing through the synapses and dendritic tree, then summed. It approximately obeys the differential equation [12,18]

$$D_{\alpha\beta}V_e(\mathbf{r},t) = \nu_{ae}\phi_e(\mathbf{r},t) + \nu_{ai}\phi_i(\mathbf{r},t) + \nu_{as}\phi_s(\mathbf{r},t-t_0/2), \tag{2}$$

$$D_{\alpha\beta} \equiv \left[\frac{1}{\alpha\beta}\frac{d^2}{dt^2} + \left(\frac{1}{\alpha}+\frac{1}{\beta}\right)\frac{d}{dt} + 1\right], \tag{3}$$

where α and β are the mean decay and rise rates, respectively, of the cell-body potential produced by an impulse at dendritic synapses and $\beta\approx 4\alpha$. The right-hand side of Eq. (2) involves contributions from $\phi_{e,i}$, from other cortical neurons, and inputs ϕ_s from thalamic relay nuclei, delayed by a time

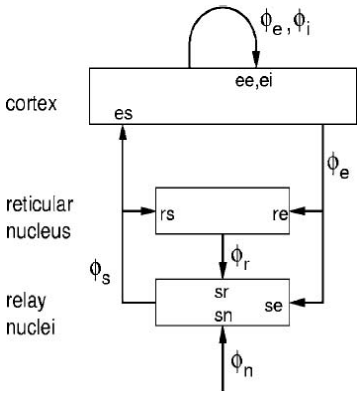

FIG. 1. Schematic of corticothalamic interactions, showing locations ab at which ν_{ab} and G_{ab} act.

$t_0/2$ required for signals to propagate from thalamus to cortex. In Eq. (2), $\nu_{ab}=N_{ab}s_{ab}$, where N_{ab} is the mean number of synapses from neurons of type $b=e,i,s$ to type $a=e,i$ and s_{ab} is the strength of the response to a unit signal from neurons of type b.

Each part of the corticothalamic system produces a field ϕ_a of pulses that travels at a velocity v_a (e.g., for excitatory neurons $v_e\approx 10$ m s^{-1}) and obeys a damped wave equation [11,12,18]

$$\left(\frac{1}{\gamma_a^2}\frac{\partial^2}{\partial t^2} + \frac{2}{\gamma_a}\frac{\partial}{\partial t} + 1 - r_a^2\nabla^2\right)\phi_a(\mathbf{r},t) = S[V_a(\mathbf{r},t)], \tag{4}$$

where γ_a is the mean decay rate and r_a is the mean range of axons a. If intracortical connectivities are proportional to the numbers of synapses involved, $V_i=V_e$ and $Q_i=Q_e$ [10,18], which lets us concentrate on excitatory quantities. The smallness of r_i also lets us set $\gamma_i\approx\infty$ and $r_i\approx 0$ [12].

The model incorporates corticothalamic connectivities and thalamic nonlinearities. Figure 1 shows the connectivities considered, including the thalamic reticular nucleus that inhibits relay nuclei. The latter relay external stimuli ϕ_n to the cortex as well as corticothalamic feedback. The cell-body potentials then satisfy

$$D_{\alpha\beta}V_c(\mathbf{r},t) = \nu_{ce}\phi_e(\mathbf{r},t-t_0/2) + \nu_{cs}\phi_s(\mathbf{r},t) + \nu_{cr}\phi_r(\mathbf{r},t) + \nu_{cn}\phi_n(\mathbf{r},t), \tag{5}$$

where there is a delay $t_0/2$ for signals to travel from cortex to thalamus or back, $c=r,s$, $\nu_{cc}=\nu_{rn}=0$, and $\phi_c(\mathbf{r},t)=S[V_c(\mathbf{r},t)]$ [18] applies because the small size of the thalamic nuclei enables us to assume $\gamma_c\approx\infty$ and $r_c\approx 0$ for $c=r,s$ in Eq. (4).

This model has 15 parameters: $Q_{\max}$, θ, σ', α, β, t_0, ν_{ee}, ν_{ei}, ν_{es}, ν_{se}, ν_{sr}, $\nu_{sn}\phi_n$, ν_{re}, ν_{rs}, and γ_e—enough to allow realistic representation of the most salient anatomy and physiology, but few enough to yield useful interpretations. The parameters are approximately known from experiment [17,18], leading to the nominal adult human values in Table I, which are indicative only—some vary several fold between individuals, arousal states, and disorders—but are entirely compatible with physiology.

TABLE I. Physiologically plausible ranges and nominal values of parameters of the previous corticothalamic model [17].

Parameter	Range	Nominal value	Unit
$Q_{\max}$	100–1000	250	s^{-1}
θ	≈15	15	mV
σ'	≈3	3.3	mV
γ_e	70–150	100	s^{-1}
t_0	70–90	80	ms
ν_{ee}	0.05–10	1.2	mV s
$-\nu_{ei}$	0.05–10	1.8	mV s
ν_{es}	0.05–10	1.2	mV s
ν_{se}	0.05–10	1.2	mV s
$-\nu_{sr}$	0.05–10	0.8	mV s
ν_{re}	0.05–10	0.4	mV s
ν_{rs}	0.05–10	0.2	mV s
$\nu_{sn}\phi_n$	0.05–10	1.0	mV
α	25–100	50	s^{-1}
β/α	2–6	4	

III. COMPACT MODEL

In this section we derive a compact model based on the above corticothalamic model, keeping essential features of brain dynamics, such as rapid and delayed feedbacks, but approximating dendritic responses and intrathalamic dynamics. We then demonstrate, here and in Sec. IV, that many key linear and nonlinear properties of the more complex model are reproduced by the compact model in a reduced parameter space. The approximations made thus do not invalidate the compact model, and it is thus a useful tool, especially when the brain shows low-dimensional dynamics.

A. Derivation of model equations

In order to derive a compact approximation, we assume that α and β are large relative to d/dt so that we can write $D_{\alpha\beta}\approx 1$ in Eq. (3). This nominally restricts analysis to angular frequencies $\omega \lesssim \alpha,\beta$, corresponding to a frequencies of $\lesssim$10 Hz. However, the analysis is expected to be semiquantitatively correct even somewhat above this point and it is a matter for verification which dynamical features are, in fact, preserved. We turn to the question of verification below.

Using the approximations $V_i=V_e$ [10,18], $\gamma_a\approx\infty$, and $r_a \approx 0$ $(a=i,r,s)$ [12,18] from Sec. II, Eqs. (2), (4), and (5) yield a single nonlinear equation for $V_e(\mathbf{r},t)$:

$$\begin{aligned} V_e(\mathbf{r},t) - \nu_{ei}S[V_e(\mathbf{r},t)] - \nu_{ee}\phi_e(\mathbf{r},t) \\ = \nu_{es}S\Big\{ \nu_{se}\phi_e(\mathbf{r},t-t_0) + \nu_{sn}\phi_n(\mathbf{r},t-t_0/2) \\ + \nu_{sr}S\Big[\nu_{re}\phi_e(\mathbf{r},t-t_0) + \frac{\nu_{rs}}{\nu_{es}}\{V_e(\mathbf{r},t) - \nu_{ei}S[V_e(\mathbf{r},t)] \\ - \nu_{ee}\phi_e(\mathbf{r},t)\}\Big]\Big\}. \end{aligned} \tag{6}$$

Solving this transcendental equation for $S(V_e)$, we obtain the formal solution

$$S[V_e(\mathbf{r},t)] = f(\phi_e(\mathbf{r},t),\phi_e(\mathbf{r},t-t_0),\phi_n(\mathbf{r},t-t_0/2)), \tag{7}$$

in terms of a function f that only depends on $\phi_e(\mathbf{r},t)$, $\phi_e(\mathbf{r},t-t_0)$, and $\phi_n(\mathbf{r},t-t_0/2)$. In Secs. III C and III D we find approximate explicit expressions to replace Eqs. (6) and (7).

Inserting Eq. (7) into Eq. (4), we obtain a single time-delayed differential equation with one variable ϕ_e:

$$\begin{aligned} \frac{1}{\gamma_e^2}\frac{\partial^2\phi_e(\mathbf{r},t)}{\partial t^2} + \frac{2}{\gamma_e}\frac{\partial\phi_e(\mathbf{r},t)}{\partial t} - r_e^2\nabla^2\phi_e(\mathbf{r},t) \\ = -\phi_e(\mathbf{r},t) + f(\phi_e(\mathbf{r},t),\phi_e(\mathbf{r},t-t_0),\phi_n(\mathbf{r},t-t_0/2)). \end{aligned} \tag{8}$$

Compared with the more complex corticothalamic model in the previous section, this compact model requires only ϕ_e to describe the brain activity, which implies that the brain dynamics can be studied in a reduced space under certain conditions. In fact, ϕ_e is known to be the most relevant variable to EEG's [9,12] and functional magnetic resonance imaging [24]. We note that the right-hand side of Eq. (8) depends on only three quantities with clear physiological meanings: $\phi_e(\mathbf{r},t)$ represents activities due to nearby neurons, $\phi_e(\mathbf{r},t-t_0)$ denotes delayed feedbacks via extracorticocortical loop, and the external stimulus is $\phi_n(\mathbf{r},t-t_0/2)$. Here the delay time of the external stimulus is $t_0/2$ since the stimulus is relayed to cortex via a half pathway.

B. Steady states and stability

Since low-dimensional highly synchronized solutions are of most interest here, we assume for the moment that the system is spatially homogenous so that the solution is independent of spatial coordinates. That is, the Laplacian term in Eq. (8) is set to zero. We now decompose the second-order equation (8) into two first-order equations, introduce $\mathbf{v}=(\phi_e,d\phi_e/d\tau)^T=(v_1,v_2)^T$, and rescale time by the decay rate, giving a new time variable $\tau=\gamma_e t$. Then, combined with Eq. (7), the model equation (8) becomes

$$\frac{d\mathbf{v}}{d\tau} = \begin{pmatrix} v_2 \\ -v_1 + f(v_1,\hat{v}_1,\hat{\phi}_n) - 2v_2 \end{pmatrix}, \tag{9}$$

where $\hat{v}_1(\tau)=v_1(\tau-\tau_0)$ and $\hat{\phi}_n(\tau)=\phi_n(\tau-\tau_0/2)$. Then, the steady states of the compact model can be obtained by setting $d\mathbf{v}/d\tau$ to zero in Eq. (9). Since $\tau_0=0$, $\hat{\mathbf{v}}=\mathbf{v}=\mathbf{v}^*$ in a steady state, we obtain a steady state $\mathbf{v}^*=(v_1^*,0)$ where v_1^* satisfies $v_1^*=f(v_1^*,v_1^*,\hat{\phi}_n)$. For example, Fig. 2 shows the fixed points obtained numerically from Eq. (6) as functions of the parameter ν_{se} in a physiologically plausible range. Depending on the parameter value, the model has one ($\nu_{se}\lesssim 0.9$ or $\nu_{se}\gtrsim 4.6$) or three fixed points ($0.9\lesssim\nu_{se}\lesssim 4.6$). The trajectories of the fixed points (see L_1-L_3 in Fig. 2) indicate that there exists a stable zone. Note that we obtain similar results with other parameters (e.g., ν_{ee}). We set all time derivatives to zero in Eq. (6) to derive steady states. This is the

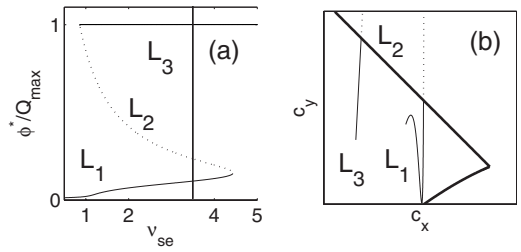

FIG. 2. Fixed points and their stability: (a) ϕ_e^* vs ν_{se} and (b) fixed points L_1-L3 in a parameter space where stable fixed points (solid curves L_1 and L_3) are confined within a stable zone (surrounded by thick solid lines) and unstable fixed points (dotted curves L_2) are located outside the zone. Note that the two parts of curve L_2 in (b) join at large c_y (not shown), making it a solid curve. The multiple fixed points merge smoothly at the critical values $\nu_{se} \approx 0.9, 4.6$. The apparent sharp corner at upper left in (a) proves to be smooth at higher resolution.

same as setting $d/dt=0$ and $\partial/\partial t=0$ in Eqs. (3) and (4), as done in the previous model [22] to derive steady states. Hence, the compact model has the same steady states as the more general model.

When we linearize Eq. (9) about the steady states, we need to consider two terms separately: $\mathbf{v}(\tau)$ a term without the delay and $\mathbf{v}(\tau-\tau_0)$ with the delay. Considering a small deviation from the steady state $\bar{\mathbf{v}}=\mathbf{v}-\mathbf{v}^*$, where $\mathbf{v}^*$ is the steady state, Eq. (9) becomes

$$\frac{d\bar{\mathbf{v}}}{d\tau} = \begin{pmatrix} 0 & 1 \\ c_1 & -2 \end{pmatrix} \bar{\mathbf{v}}(\tau) + \begin{pmatrix} 0 & 0 \\ c_2 & 0 \end{pmatrix} \bar{\mathbf{v}}(\tau-\tau_0), \tag{10}$$

where $c_1 = -1 + \partial f/\partial v_1|_{\mathbf{v}=\mathbf{v}^*}$ and $c_2 = \partial f/\partial \hat{v}_1|_{\mathbf{v}=\mathbf{v}^*}$, which are dimensionless coefficients. We now seek solutions of the form $\bar{\mathbf{v}}(\tau)=\mathbf{v}_0 e^{\lambda\tau}$. Substituting this into Eq. (10), we obtain

$$\lambda \mathbf{v}_0 = \begin{pmatrix} 0 & 1 \\ c_1 + c_2 e^{-\lambda\tau_0} & -2 \end{pmatrix} \mathbf{v}_0 = D\mathbf{J}\mathbf{v}_0. \tag{11}$$

Nontrivial solutions $\mathbf{v}_0 \neq 0$ of Eq. (11) exist when $\det(D\mathbf{J}-\lambda\mathbf{I})=0$ and can thus be obtained by solving the characteristic equation

$$\lambda^2 + 2\lambda - c_1 = c_2 e^{-\lambda\tau_0}. \tag{12}$$

The stability of the nontrivial solutions is determined by the real parts of the solutions of Eq. (12). For example, if there is no time delay ($\tau_0=0$), the solutions are $\lambda_\pm = -1 \pm \sqrt{1+c}$, where $c=c_1+c_2$. Therefore, the steady state is unstable if $c>0$. Thus, $c_1+c_2=0$ is an instability boundary for the slow wave ($\sim$0 Hz). In addition, for $\tau_0>0$, there exists another condition for Eq. (12) to have a solution with zero real part. At this point the steady state becomes a limit cycle, which implies that a Hopf birfucation may occur at the instability boundary. Substituting $\lambda=i\omega$ into Eq. (12), we obtain

$$-\omega^2 - c_1 = c_2 \cos(\omega\tau_0), \tag{13}$$

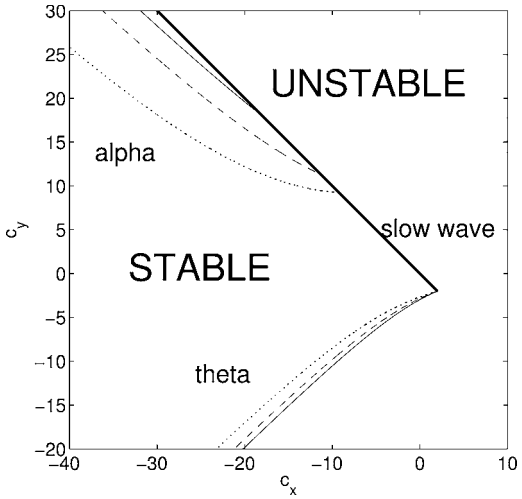

FIG. 3. Stability zone (inside the "wedge") in the c_x-c_y parameter space for given τ_0. The slow-wave boundary (thick solid line) is independent of τ_0, while boundaries corresponding to the frequencies of the α ($\sim$10 Hz) and θ ($\sim$3 Hz) instabilities are partly determined by τ_0: thin solid line ($\tau_0=8$), dashed line ($\tau_0=4$), and dotted line ($\tau_0=2$). Note that $c_{1,2}$ are rescaled by τ_0 [i.e., $c_{x,y}=\tau_0 c_{1,2}$ so that the θ and slow-wave boundaries have the fixed vertex at $(c_x,c_y)=(2,-2)$].

$$2\omega = -c_2 \sin(\omega\tau_0). \tag{14}$$

Thus, when $\omega>0$, the instability boundaries can be obtained as parametric curves of ω in c_1-c_2 space for given τ_0. Defining $c_{x,y}=c_{1,2}\tau_0$ and $\psi=\omega\tau_0$, Eqs. (13) and (14) become

$$c_x = 2\psi/\tan\psi - \psi^2/\tau_0, \tag{15}$$

$$c_y = -2\psi/\sin\psi. \tag{16}$$

Note that $c_x \to 2$ and $c_y \to -2$ as $\psi \to 0$, which is the vertex of the stable zone in Fig. 3. Now the instability boundaries are parametrically determined by ψ. When $\psi \leq \pi$, the instability boundary lies at $c_y<0$, whereas $c_y>0$ for $\pi<\psi\leq 2\pi$ as shown in Fig. 3.

This stability zone of the compact model is very similar to the three-dimensional "tent-shaped" stability zone of the previous model [17], but reduced to two gain-related dimensions. In the previous work stability boundaries were parametrized in a reduced space with cortical (x), corticothalamic (y), and thalamic (z) coordinates. As we show in the following section, the parameters c_x and c_y of the compact model can be obtained from the previous model and correspond to $\gamma_e t_0(x-1)$ and $\gamma_e t_0 y$, respectively. However, there is no correspondence to the thalamic stability parameter z, since intrathalamic feedbacks are not considered in the compact model ($z=0$). The previous x, y, and z coordinates were bounded (e.g., $0 \leq x \leq x_c \approx 1.2$, which corresponds to $-8 \leq c_x \lesssim 2$ for the parameters in Table I), based on physiological observations, but we allow c_x and c_y to vary more widely to explore the model's properties more extensively here. As an interesting result of this exploration, we find the α instability boundaries in the zone with $c_y \gtrsim 8$ and $c_x \lesssim -8$, which were previously reported on only the $z>0$ surface of the

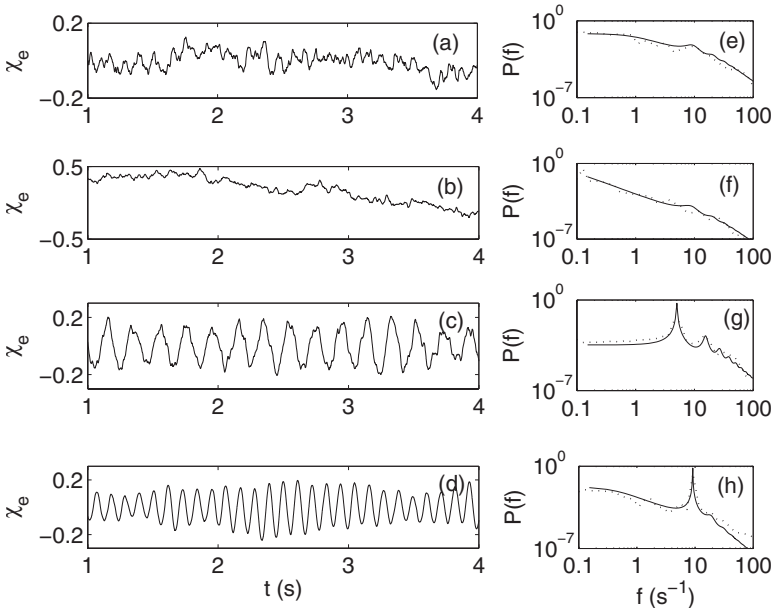

FIG. 4. Typical stable time series (a)–(d) and corresponding power spectra (e)–(h) of the linearized model: (a) and (e) with nominal values ($c_1=-0.49$ $c_2=0.27$) obtained from Table I, (b) and (f) near the slow-wave instability boundary, (c) and (g) near the θ instability boundary, (d) and (h) near the α instability boundary. Numerically obtained spectra (dotted lines) are compared with the analytic predictions (solid lines) [see Eq. [18]].

"tent" diagram [17] for c_x restricted to $c_x \gtrsim -8$ ($x \gtrsim 0$). However, the α instability of the previous model is also found to meet the slow-wave instability at $z=0$ when $x<0$. This shows that the topological structure of the stable zone is qualitatively similar to the structure of "tent" zone, but quantitatively slightly different. We also note that the delay time τ_0 is also a key parameter that affects the stability, as shown in Fig. 3.

C. Simplified linear model and linear spectra

In order to study linear dynamics near steady states and verify they reproduce those of previous models, we linearize Eq. (8) in the vicinity of a steady state, which gives (see Appendix A for details)

$$\frac{\partial^2 \chi_e(\mathbf{R},\tau)}{\partial \tau^2} + 2\frac{\partial \chi_e(\mathbf{R},\tau)}{\partial \tau} - \nabla_{\mathbf{R}}^2 \chi_e(\mathbf{R},\tau) = +c_1\chi_e(\mathbf{R},\tau) + c_2\chi_e(\mathbf{R},\tau-\tau_0) + c_3\chi_n(\mathbf{R},\tau-\tau_0/2), \tag{17}$$

where $\tau=\gamma_e t$ is the dimensionless time unit, $\chi_a=\bar{\phi}_a/Q_{\max}$ is a dimensionless field, and $\mathbf{R}=\mathbf{r}/r_e$ is a dimensionless spatial vector so that $\nabla_{\mathbf{R}}^2=r_e^2\nabla^2$ is a dimensionless Laplacian. The coefficients are explicitly determined [see Eq. (A10)–(A12)] using nominal parameter values of the previous corticothalamic model [17] (see Table I) and numerically obtained steady-state values (see Fig. 2), which are $c_1\sim-0.49$, $c_2\sim0.27$, and $c_3\sim0.09$.

The physiological meanings of each term in the linearized compact model equation (17) can be clearly understood. The first term represents rapid corticocortical feedbacks, while the second term represents feedback via extracortical pathways delayed by a time τ_0. We therefore argue that c_1 parametrizes the strength of corticocortical activities, c_2 parametrizes corticothalamic feedbacks, and c_3 parametrizes a delayed external stimulus that can be considered as random noise in many cases; we set the last term of Eq. (17) to be small-amplitude uniformly distributed random noise for the rest of this paper in numerical simulations.

Spectra of the linearized compact model can be easily obtained by converting the model equation (17) into the frequency domain using a Fourier transformation. The transfer function, which gives the cortical excitatory response per unit external stimulus, is then

$$\frac{\chi_e(\mathbf{K},\omega)}{\chi_n(\mathbf{K},\omega)} = \frac{c_3 e^{i\omega\tau_0/2}}{K^2+q^2(\omega)}, \tag{18}$$

$$q^2(\omega) = (1-i\omega)^2 - (c_1+1) - c_2 e^{i\omega\tau_0}, \tag{19}$$

where $\mathbf{K}$ is the dimensionless wave vector corresponding to $\mathbf{R}$. In the case of a random external stimulus, $|\chi_n(\mathbf{K},\omega)|$ is a constant and $P(\mathbf{K},\omega)\sim|\chi_e(\mathbf{K},\omega)|^2$. The power spectrum can be written as

$$P(\omega) \sim \int \frac{d\mathbf{K}}{|\mathbf{K}^2+q^2(\omega)|^2}, \tag{20}$$

which is analytically integrable [12,17], giving

$$P(\omega) \sim \begin{cases} \dfrac{1}{|q^2|\mathrm{Re}\, q}, \\ \left|\dfrac{\mathrm{Arg}\, q^2}{\mathrm{Im}\, q^2}\right|, \end{cases} \tag{21}$$

for one- and two-dimensional systems, respectively, where Arg denotes the complex argument and Re and Im denote the real and imaginary parts, respectively. This result reproduces previous work [17,18] in the limit $\alpha,\beta\to\infty$. If we consider a spatially homogeneous system, the power spectrum satisfies $P(\omega)\sim 1/|q^2(\omega)|^2\sim\omega^{-4}$ ($\omega\gg1$), which is shown in Fig. 4 in comparison with the numerically obtained power spectrum of the linearized model.

D. Simplified nonlinear model

Given the compact model (8), the linearized equation (17) is a good tool to study some properties, but its solutions are well defined in the stable region only and diverge in the unstable region. In addition, nonlinear properties (e.g., limit cycles and bifurcations) are observed. To treat these phenomena we retain the next-order nonlinear terms beyond the linearized approximation. Iteratively expanding Eq. (7) up to cubic terms, Eq. (8) yields the explicit form [which also avoids the difficulties of the transcendental equation (6)]

$$\frac{\partial^2 \chi_e(\mathbf{R},\tau)}{\partial \tau^2} + 2\frac{\partial \chi_e(\mathbf{R},\tau)}{\partial \tau} - \nabla_{\mathbf{R}}^2 \chi_e(\mathbf{R},\tau) = +h_1\chi_e(\mathbf{R},\tau) + h_2\chi_e(\mathbf{R},\tau-\tau_0) + \epsilon_2\chi_e^2(\mathbf{R},\tau) + \epsilon_3\chi_e^3(\mathbf{R},\tau) + h_3\chi_n(\mathbf{R},\tau-\tau_0/2), \quad (22)$$

where the coefficients h_i and ϵ_i can be related to physiology via the previous corticothalamic model [17], as discussed in Appendix B. Since the χ_e^2 term alone would make solutions of Eq. (22) diverge, we also retain the higher-order cubic term, which has a negative coefficient ($\epsilon_3<0$ since $\nu_{ei}<0$), so the solutions are bounded. For detailed derivations and an alternative nonlinear approximation, see Appendix B. Note that the right-hand side of Eq. (22) depends only on the intracortical activity (first, third, and fourth terms), the delayed corticothalamic feedback (second term), and the delayed external input (last term), as implied by Eq. (7).

Following the stability analysis in Sec. III B, we rewrite Eq. (22) as

$$\dot{\mathbf{w}} = \begin{pmatrix} w_2 \\ h_1 w_1 + \epsilon_2 w_1^2 + \epsilon_3 w_1^3 + h_2\hat{\hat{w}}_1 + h_3\hat{\chi}_n - 2w_2 \end{pmatrix}, \quad (23)$$

where $\mathbf{w}=(\chi_e, d\chi_e/d\tau)^T=(w_1,w_2)^T$, $\hat{\hat{w}}_1(\tau)=w_1(\tau-\tau_0)$, and $\hat{\chi}_n(\tau)=\chi_n(\tau-\tau_0/2)$. The mean of the external stimulus has been incorporated in determining the fixed points, so $\langle\chi_n\rangle=0$. Assuming χ_n to be random white noise and setting the left-hand side of Eq. (23) to zero, the fixed points occur where $w_2^*=0$ and

$$hw_1^* + \epsilon_2(w_1^*)^2 + \epsilon_3(w_1^*)^3 = 0, \quad (24)$$

where $h=h_1+h_2$. The model has one fixed point at $\mathbf{w}_0^*=(0,0)$ when $h<-\epsilon_2^2/4|\epsilon_3|$, while it has multiple fixed points at $\mathbf{w}_0^*=(0,0)$ and $\mathbf{w}_\pm^*=(w_\pm^*,0)=((-\epsilon_2\pm\sqrt{\epsilon_2^2-4h\epsilon_3})/2\epsilon_3,0)$ when $h\geqslant-\epsilon_2^2/4|\epsilon_3|$. (For simplicity of analysis we set $\epsilon_2>0$ without loss of generality.) These fixed points are drawn in Fig. 5(a) as functions of h, where solid curves denote stable fixed points and dotted curves denote unstable ones.

The stability of the fixed points is determined by the modified characteristic equation

$$\lambda^2 + 2\lambda - h_1 - 2\epsilon_2 w_1^* - 3\epsilon_3(w_1^*)^2 = h_2 e^{-\lambda\tau_0} \quad (25)$$

at the fixed points. When $\tau=0$, the stability of the fixed points can be evaluated from the eigenvalues of Eq. (25), setting $\tau_0=0$. The eigenvalues are as follows: (i) At $\mathbf{w}_0^*$,

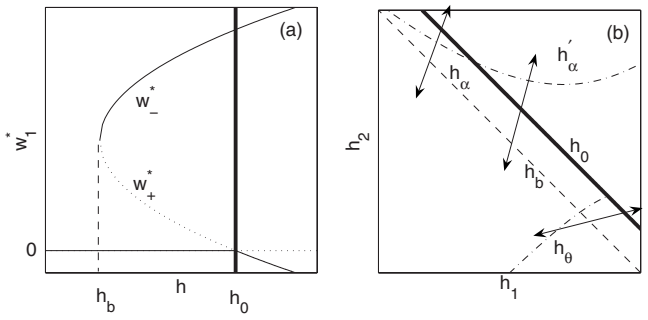

FIG. 5. Schematic of bifurcation: (a) Stable fixed points (solid lines) and unstable fixed points (dotted lines) are calculated with respect to h. (b) Locations of h values in h_1-h_2 parameter space, where h_θ, h_α, h'_α, and $h_0=0$ are instability boundaries of θ, α, and slow wave, respectively; $h_b=-\epsilon_2^2/4|\epsilon_3|$ is the critical h (saddle node) where nontrivial fixed points emerge. Double-pointed arrows denote typical pathways when the system crosses the instability boundaries. For example, the bottom right double-pointed arrow indicates a case when the system crosses the θ instability boundary, the saddle-node critical point, and the slow-wave instability.

$$\lambda_+ = -1 + \sqrt{1+h}. \quad (26)$$

Thus the fixed point is stable (unstable) when $h<0$ ($h>0$) as seen in Fig. 5(a), where $\mathbf{w}_0^*$ is drawn as a solid line (stable) for $h<0$ and dotted line (unstable) for $h>0$. (ii) At $\mathbf{w}_\pm^*$,

$$\lambda_+ = -1 + \sqrt{1+(\epsilon_2^2-4h\epsilon_3 \mp \epsilon_2\sqrt{\epsilon_2^2-4h\epsilon_3})/2\epsilon_3}. \quad (27)$$

Thus $\mathbf{w}_\pm^*$ is stable when $h>0$ [see the two solid curves in Fig. 5(a) for $h>0$], while $\mathbf{w}_-^*$ ($\mathbf{w}_+^*$) is stable (unstable) when $-\epsilon_2^2/4|\epsilon_3|<h<0$ [solid and dotted curves, respectively, in Fig. 5(a) for $h<0$].

When $\tau\neq0$, nontrivial oscillating solutions near the fixed points can exist. Since we consider small perturbations from the linearized model, Eq. (25) has similar solutions to Eq. (12). Thus, the instability boundaries for limit-cycle solutions are given by Eqs. (15) and (16) upon replacing $c_{1,2}$ with $h_{1,2}$ (i.e., $c_1\to h_1+2\epsilon_2 w_1+3\epsilon_3 w_1^2$ and $c_2\to h_2$).

IV. DYNAMICS OF EPILEPTIC SEIZURES

We now consider the dynamics of epileptic seizures to further illustrate the application of our model, verify that it reproduces the nonlinear dynamical properties of more complex formulations, and show how it yields additional insights. Stable limit-cycle signals are commonly observed in many EEG recordings during epileptic seizures [3]. In particular, the generalized absence (petit mal) epilepsy shows limit-cycle behavior at around 3 Hz for 10–20 s. Although the dynamical origin of seizures is not fully understood, recent work has suggested that bifurcations of steady states under certain conditions may lead to seizure activity [17,20]. We thus examine possible bifurcations and illustrate resulting epileptic seizures using our simplified nonlinear model (22). The limit-cycle periods are also estimated analytically in Sec. IV B.

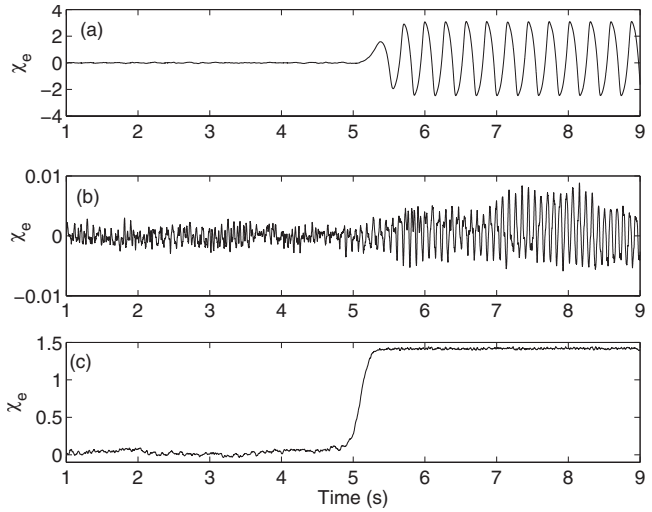

FIG. 6. Bifurcations of steady states when they cross the instability boundaries: (a) the θ, (b) the α, and (c) the slow-wave instability boundary. The system initially stays inside the stability zone and becomes unstable after it crosses an instability boundary at $t=5$.

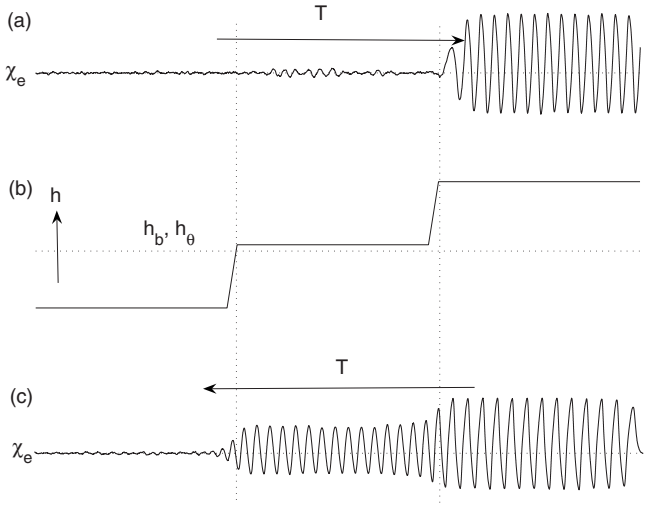

FIG. 7. Hysteresis at the θ instability boundary. (a) and (c) show time series of Eq. (22), which are small deviations χ_e from steady states of ϕ_e, while (b) shows how a parameter h is varying during the numerical integrations. The different time series in the region II indicate a hysteresis in the parameter regime $h_\theta < h < h_0$. Note that the time axis in (c) is reversed. For definitions of h, h_b, and h_θ, refer to Fig. 5.

A. Limit cycles and hysteresis

In previous literature, the dynamical origin of seizures was related to the stability diagram [17] analogous to Fig. 3, and some explorations of EEG's during seizures have also been reported [20]. Similarly, our model shows limit-cycle solutions when the system crosses either the θ or α instability boundaries, which is consistent with seizure activity being related to sudden changes of the stability of a brain. These limit cycles are caused by varying model parameters that represent underlying physiology. Although it is of interest to study which physiological mechanisms precipitate the instability and how the model parameters are affected by them, this is beyond the scope of the present work.

We follow the earlier arguments in [17,20], which show that epileptic seizures are caused by bifurcations of steady states of a system when it crosses the instability boundaries. As shown in Fig. 6, we observe three different cases: (i) transition to another fixed point when the system crosses the slow-wave instability boundary, (ii) a limit cycle around 3 Hz when it crosses the θ instability boundary, and (iii) a limit cycle around 10 Hz when it crosses the α instability boundary. The periods of the limit cycles (ii) and (iii) are analytically estimated in Sec. IV B.

Figure 7 illustrates hysteresis at onset of seizure activity, which occurs when a system crosses limit-cycle instability boundary [e.g., see the double arrow in Fig. 5(b)]. When h_b and h_θ are very close, the system can have multiple attractors near the instability region and the numerical solutions are determined by initial conditions. The system has a single fixed point at zero perturbation below the boundaries, but it has a limit-cycle attractor above h_θ. Thus, the system has different initial conditions when it crosses the instability region, depending on the direction, and, as a result, has different numerical solutions as seen in Fig. 7. However, when $h_b \gg h_\theta$ the system has only a single attractor in each region: a fixed point ($h < h_\theta$) and a limit cycle ($h > h_\theta$), respectively. The system thus cannot show any hysteresis.

B. Estimates of limit-cycle periods during seizures

The limit-cycle period during seizures can be easily estimated using the compact model with the phase $\psi_0 = \omega\tau_0 = 2\pi t_0/T$ in Eq. (16), which is evaluated as a function of c_y in the following paragraphs.

(i) At the vertex of the stability zone ($0 < \psi_v \ll 1$), we obtain $\psi_v \approx \sqrt{-3(2+c_y)}$ (for $c_y \lesssim -2$) from Eq. (16):

$$T_v = \frac{2\pi t_0}{\psi_v} \approx \frac{2\pi t_0}{\sqrt{-3(2+c_y)}}. \tag{28}$$

Thus $T_v \to \infty$ as $c_y \to -2$, which implies a transition to another fixed point near the vertex.

(ii) The θ instability occurs when $0 < \psi < \pi$. We thus set $\psi_\theta = \pi/2 \pm \delta$, then obtain $c_y \sim -2\psi_\theta \sim -\pi$ from Eq. (16) and

$$T_\theta = 2\pi t_0/\psi_\theta \approx -4\pi t_0/c_y \sim 4t_0. \tag{29}$$

In particular, when $t_0 = 80$ ms, the resonance period of the θ instability is $T_\theta \sim 320$ ms, which matches well with experimentally reported values of 200–400 ms [3]. According to previous theoretical work, the period of the absence (petit mal) instability was estimated to be $T_\theta \approx 2t_0 + 6/\alpha + 6/\beta + 4/\gamma_e$ [17]. For the nominal values in Table I, the period is roughly $T_\theta \sim 350$ ms, which is also compatible with our result. In this parameter regime, $1/2\alpha \sim 2/\beta \sim 1/\gamma_e \sim 0.1t_0$ for the nominal values. Thus the period is approximately $3.9t_0$, which is roughly equal to our result $4.0t_0$. The coefficient of t_0 was 2 in the previous estimate, but when t_0 is sufficiently large, the θ instability occurs at $c_y \ll -2$ and $\psi_\theta \sim \pi$, giving $T_\theta \sim 2\pi t_0/\phi_\theta \sim 2t_0$, which is the same as the previous estimate in the relevant limit $\alpha, \beta, \gamma_e \to \infty$.

(iii) The α instability occurs when $\pi<\psi<2\pi$. We define ψ^* to be the angle where c_y in Eq. (16) has a minimum ($\psi^* \approx 4.50 \approx 1.43\pi$) and $\psi_\alpha = \psi^* \pm \delta = 3\pi/2 + \bar{\delta}$ ($\bar{\delta} = \pm\delta - 0.07\pi$). From Eq. (16), $\sin\psi_\alpha \sim -\cos\bar{\delta} \sim -1 + \bar{\delta}^2/2$ and $\psi_\alpha \sim c_y(1 - \bar{\delta}^2/2)/2$, so

$$T_\alpha = 2\pi t_0/\psi_\alpha \approx 4\pi t_0/[c_y(1-\bar{\delta}^2/2)] \approx 4.10\pi t_0/c_y. \quad (30)$$

Since $c_y \approx 2\psi^*/(1-\bar{\delta}^2/2) \sim 2.93\pi$ at the α instability boundary, $T_\alpha \approx 1.40 t_0 \sim 110$ ms when $t_0 = 80$ ms, which matches well with the period of tonic-clonic (grand mal) seizures [3] and previous theoretical work where the period of α rhythm was estimated to be $T_\alpha \approx t_0 + 1/\alpha + 1/\beta$ [15]. With nominal values (see Table I), $1/4\alpha \sim 1/\beta \sim 0.05 t_0$ and $T_\alpha \approx 1.25 t_0$, which is close to our result. Similarly, when t_0 is sufficiently large, the α instability occurs at $c_y \gg -2$ and $\psi_\alpha \sim 2\pi$, and we obtain $T_\alpha \sim 2\pi t_0/\phi_\alpha \sim t_0$, which is the same as the previous estimate in the relevant limit $\alpha, \beta \to \infty$.

V. SUMMARY AND DISCUSSION

The chief result of this work is that we have developed a compact model which is derived from a physiologically based mean-field model of corticothalamic dynamics by approximating the dendritic responses and intrathalamic feedbacks. This model describes brain dynamics using a single second-order delay differential equation to replace a set of four such equations in the original formulation, but still involves solution of a transcendental equation. Later in the paper explicit linear and approximate nonlinear forms are derived that enable the dynamics to be investigated in the neighborhood of fixed points. The simplified model can be expressed via just three physiologically intuitive feedback terms, covering corticocortical connections, delayed feedbacks via extracortical paths, and the delay inherent in the latter loop. It involves only one explicit activity variable and can thus be straightforwardly used to follow activity in a reduced parameter space.

We verified that the compact model successfully reproduces key linear and nonlinear properties of brain dynamics from both experiments and models, notwithstanding the approximations made. In particular, the spectral peaks of EEG's, such as those of slow-wave, θ and α peaks, are observed for physiologically plausible parameters. The sensitivity of these frequencies to the model parameters is explored and explained. As a result, we found a stability zone in our model parameter space and compared it with previous work [17,20]. As a system crosses the stability boundaries, limit cycles occur, which may lead to seizure activity. In addition, the limit-cycle periods during seizures were analytically estimated and shown to be consistent with physiologically observed values and previous work. The estimated period at the θ instability ($\sim$300 ms) corresponds well to the period of absence (petit mal) seizures (200–400 ms). Limit cycles with a period of $\sim$100 ms are also predicted beyond the α instability boundary, consistent with the period of tonic-clonic (grand mal) seizures [3].

Although some previous continuum models (e.g., Ref. [17]) describe brain activity in more physiological detail, they involve several variables and ten or more parameters. As a result, it is very hard to investigate the properties of these models systematically (numerical approaches are possible but are still seriously hampered by the high dimensionality of parameter space). Using our compact formulation, many key properties of the brain can be described in a simplified way with fewer parameters, especially when it exhibits low-dimensional dynamics. With the help of this compact formulation, we can thus analyze the basic brain dynamics more systematically, which will provide useful guidance for investigation of more complex models and neuroscience applications, just as simplified neuronal models serve to guide more complex and accurate conductance-based ones at the microscopic level.

ACKNOWLEDGMENTS

The authors thank J.A. Roberts for helpful comments on the manuscript. This work was supported by the Australian Research Council.

APPENDIX A: LINEAR COMPACT MODEL

In this appendix we derive the linearized model from the compact model (8). Assuming that the system is spatially homogenous and $D_{\alpha\beta} \equiv 1$, we obtain the following three nonlinear equations from Eqs. (2) and (5):

$$V_e(t) = \nu_{ee}\phi_e(t) + \nu_{ei}S[V_e(t)] + \nu_{es}S[V_s(t-t_0/2)], \quad (A1)$$

$$V_r(t) = \nu_{re}\phi_e(t-t_0/2) + \nu_{rs}S[V_s(t)], \quad (A2)$$

$$V_s(t) = \nu_{se}\phi_e(t-t_0/2) + \nu_{sr}S[V_r(t)] + \nu_{sn}\phi_n(t). \quad (A3)$$

Since dynamical behaviors near steady states are of most interest, we let $Q_a = S(V_a)$, $q_a = Q_a - Q_a^*$, and $\bar{\phi}_a = \phi_a - \phi_a^*$, where $Q_a^* = S(V_a^*)$ and ϕ_a^* are the steady-state values, and simplify the inverse sigmoidal function on the left-hand side of Eqs. (A1)–(A3) using

$$V_a = S^{-1}(Q_a) = S^{-1}(Q_a^*) + \frac{\sigma'}{Q_a^*(1-Q_a^*/Q_{\max})}q_a + O(q_a^2). \quad (A4)$$

We thus obtain

$$q_e^{(1)}(t) = \mu_{ee}\bar{\phi}_e(t) + \mu_{ei}q_e^{(1)}(t) + \mu_{es}q_s^{(1)}(t-t_0/2), \quad (A5)$$

$$q_r^{(1)}(t) = \mu_{re}\bar{\phi}_e(t-t_0/2) + \mu_{rs}q_s^{(1)}(t), \quad (A6)$$

$$q_s^{(1)}(t) = \mu_{se}\bar{\phi}_e(t-t_0/2) + \mu_{sr}q_r^{(1)}(t) + \mu_{sn}\bar{\phi}_n(t), \quad (A7)$$

where $\mu_{ab} = (\nu_{ab}/\sigma')[Q_a^*(1-Q_a^*/Q_{\max})]$ and $q_a^{(1)}$ denotes the approximated value of q_a considering linear terms only. Eliminating $q_s^{(1)}$ and $q_r^{(1)}$ from Eqs. (A5)–(A7), we obtain

$$q_e^{(1)}(t) = \frac{\mu_{ee}}{1-\mu_{ei}}\bar{\phi}_e(t) + \frac{\mu_{es}(\mu_{se}+\mu_{sr}\mu_{re})}{(1-\mu_{ei})(1-\mu_{sr}\mu_{rs})}\bar{\phi}_e(t-t_0) + \frac{\mu_{es}\mu_{sn}}{(1-\mu_{ei})(1-\mu_{sr}\mu_{rs})}\bar{\phi}_n(t-t_0/2). \quad (A8)$$

Substituting Eq. (A8) into the right-hand side of Eq. (8), we finally obtain the linearized equation

$$\frac{\partial^2 \chi_e(\mathbf{R},\tau)}{\partial \tau^2} + 2\frac{\partial \chi_e(\mathbf{R},\tau)}{\partial \tau} - \nabla_{\mathbf{R}}^2 \chi_e(\mathbf{R},\tau) = c_1 \chi_e(\mathbf{R},\tau) + c_2 \chi_e(\mathbf{R},\tau - \tau_0) + c_3 \chi_n(\mathbf{R},\tau - \tau_0/2), \tag{A9}$$

where $\tau = \gamma_e t$ is a dimensionless time, $\chi_a = \bar{\phi}_a / Q_{\max}$ is a dimensionless field, $\mathbf{R} = \mathbf{r}/r_e$ is a dimensionless space vector so that $\nabla_{\mathbf{R}}^2 = r_e^2 \nabla^2$, and the coefficients are

$$c_1 = -1 + \frac{\mu_{ee}}{1 - \mu_{ei}}, \tag{A10}$$

$$c_2 = \frac{\mu_{es}(\mu_{se} + \mu_{sr}\mu_{re})}{(1 - \mu_{ei})(1 - \mu_{sr}\mu_{rs})}, \tag{A11}$$

$$c_3 = \frac{\mu_{es}\mu_{sn}}{(1 - \mu_{ei})(1 - \mu_{sr}\mu_{rs})}. \tag{A12}$$

APPENDIX B: NONLINEAR MODEL WITH A CUBIC TERM

Expanding the left-hand side of Eq. (A1) up to cubic terms, Eq. (A5) becomes

$$q_e(t) + \eta_{e2} q_e^2(t) + \eta_{e3} q_e^3(t) = \mu_{ee} \bar{\phi}_e(t) + \mu_{ei} q_e(t) + \mu_{es} q_s(t - t_0/2), \tag{B1}$$

where the coefficients are

$$\eta_{e2} = \frac{2Q_e^* - Q_{\max}}{Q_e^*(Q_{\max} - Q_e^*)}, \tag{B2}$$

$$\eta_{e3} = \frac{2[3(Q_e^*)^2 - 3Q_e^* Q_{\max} + Q_{\max}^2]^2}{Q_e^*(Q_{\max} - Q_e^*)}. \tag{B3}$$

Although we have formal solutions of Eq. (B1) for q_e replacing q_s on the right-hand side with the linearized solution $q_s^{(1)}$ obtained from Eqs. (A5)–(A7), the solutions are generally too complex to be analytically useful. If $\gamma_e \gg 1/t_0$, $q_e \sim \bar{\phi}_e$ at a steady state [see Eq. (4)]. We thus further approximate Eq. (B1) by simply replacing all the q_e on the left-hand side with $\bar{\phi}_e$. Then Eq. (8) becomes

$$\frac{\partial^2 \chi_e(\mathbf{R},\tau)}{\partial \tau^2} + 2\frac{\partial \chi_e(\mathbf{R},\tau)}{\partial \tau} - \nabla_{\mathbf{R}}^2 \chi_e(\mathbf{R},\tau) = +h_1 \chi_e(\mathbf{R},\tau) + h_2 \chi_e(\mathbf{R},\tau - \tau_0) + \epsilon_2 \chi_e^2(\mathbf{R},\tau) + \epsilon_3 \chi_e^3(\mathbf{R},\tau) + h_3 \chi_n(\mathbf{R},\tau - \tau_0/2), \tag{B4}$$

where the coefficients are

$$h_1 = -1 + \frac{1 - \mu_{ee}}{\mu_{ei}}, \tag{B5}$$

$$h_2 = \frac{-\mu_{es}(\mu_{se} + \mu_{sr}\mu_{re})}{\mu_{ei}(1 - \mu_{sr}\mu_{rs})}, \tag{B6}$$

$$h_3 = \frac{-\mu_{es}\mu_{sn}}{\mu_{ei}(1 - \mu_{sr}\mu_{rs})}, \tag{B7}$$

$$\epsilon_2 = \eta_{e2}/\mu_{ei}, \tag{B8}$$

$$\epsilon_3 = \eta_{e3}/\mu_{ei}. \tag{B9}$$

An alternative form of nonlinear correction can be also derived as follows. From Eqs. (A6) and (A7) we obtain the linearized solution of q_s:

$$q_s^{(1)}(t) = \frac{\mu_{se} + \mu_{sr}\mu_{re}}{1 - \mu_{sr}\mu_{rs}} \bar{\phi}_e(t - t_0/2) + \frac{\mu_{sn}}{1 - \mu_{sr}\mu_{rs}} \bar{\phi}_n(t - t_0/2). \tag{B10}$$

Replacing t in Eq. (B10) with $t - t_0/2$ and using Eq. (A8), $V_e(t)$ in Eq. (A1) can be approximated as an explicit function of $\phi_e(t)$, $\phi_e(t - t_0)$, and $\phi_n(t - t_0/2)$. Thus,

$$V_e(t) = d_0 + d_1 \chi_e(t) + d_2 \chi_e(t - t_0) + d_3 \chi_n(t - t_0/2), \tag{B11}$$

where the coefficients are

$$d_0 = S^{-1}(\phi_e^*), \tag{B12}$$

$$d_1 = \frac{Q_{\max} \nu_{ee}}{1 - \mu_{ei}}, \tag{B13}$$

$$d_2 = \frac{Q_{\max} \nu_{es}(\mu_{se} + \mu_{sr}\mu_{re})}{(1 - \mu_{ei})(1 - \mu_{sr}\mu_{rs})}, \tag{B14}$$

$$d_3 = \frac{Q_{\max} \nu_{es}\mu_{sn}}{(1 - \mu_{ei})(1 - \mu_{sr}\mu_{rs})}. \tag{B15}$$

Substituting Eq. (B11) into Eqs. (7) and (8), the model equation becomes

$$\frac{\partial^2 \chi_e(\mathbf{R},\tau)}{\partial \tau^2} + 2\frac{\partial \chi_e(\mathbf{R},\tau)}{\partial \tau} - \nabla_{\mathbf{R}}^2 \chi_e(\mathbf{R},\tau) = -\chi_e(\mathbf{R},\tau) + \frac{1}{Q_{\max}} S[d_0 + d_1 \chi_e(\mathbf{R},\tau) + d_2 \chi_e(\mathbf{R},\tau - \tau_0) + d_3 \chi_n(\mathbf{R},\tau - \tau_0/2)]. \tag{B16}$$

Here the right-hand side includes a sigmoidal function, which is a widely used form in neuroscience.

[1] M. P. Stryker, Nature (London) **338**, 297 (1989).
[2] A. M. L. Coenen, Neurosci. Biobehav Rev. **19**, 447 (1995).
[3] E. Niedermeyer and F. H. Lopes da Silva, *Electroencephalography: Basic Principles, Clinical Applications, and Related Fields*, 4th ed. (Williams and Wilkins, Baltimore, 1999).
[4] H. R. Wilson and J. D. Cowan, Kybernetik **13**, 55 (1973).
[5] F. H. Lopes da Silva, A. Hoeks, H. Smits, and L. H. Zetterberg, Kybernetik **15**, 27 (1974).
[6] P. L. Nunez, IEEE Trans. Biomed. Eng. **21**, 473 (1974).
[7] W. J. Freeman, *Mass Action in Nervous System* (Academic, New York, 1975).
[8] M. Steriade, P. Gloor, R. R. Llinas, F. H. Lopes da Silva, and M.-M. Mesulam, Electroencephalogr. Clin. Neurophysiol. **76**, 481 (1990).
[9] P. L. Nunez, *Neocortical Dynamics and Human EEG Rhythms* (Oxford University Press, Oxford, 1995).
[10] J. J. Wright and D. T. J. Liley, Behav. Brain Sci. **19**, 285 (1996).
[11] V. K. Jirsa and H. Haken, Phys. Rev. Lett. **77**, 960 (1996).
[12] P. A. Robinson, C. J. Rennie, and J. J. Wright, Phys. Rev. E **56**, 826 (1997).
[13] P. A. Robinson, R. W. Whitehouse, and C. J. Rennie, Phys. Rev. E **68**, 021922 (2003).
[14] D. L. Rowe, P. A. Robinson, and C. J. Rennie, J. Theor. Biol. **231**, 413 (2004).
[15] P. A. Robinson, C. J. Rennie, D. L. Rowe, and S. C. O'Connor, Hum. Brain Mapp **23**, 53 (2004).
[16] P. A. Robinson, Phys. Rev. E **72**, 011904 (2005).
[17] P. A. Robinson, C. J. Rennie, and D. L. Rowe, Phys. Rev. E **65**, 041925 (2002).
[18] P. A. Robinson, C. J. Rennie, J. J. Wright, H. Bahramali, E. Gordon, and D. L. Rowe, Phys. Rev. E **63**, 021903 (2001).
[19] C. J. Rennie, P. A. Robinson, and J. J. Wright, Biol. Cybern. **86**, 457 (2002).
[20] M. Breakspear, J. A. Roberts, J. R. Terry, S. Rodigues, N. Mahant, and P. A. Robinson, Cereb. Cortex **16**, 1296 (2006).
[21] P. A. Robinson, J. Theor. Biol. **222**, 163 (2003).
[22] P. A. Robinson, C. J. Rennie, D. L. Rowe, S. C. O'Connor, J. J. Wright, E. Gordon, and R. W. Whitehouse, Neuropsychopharmacology **28**, S74 (2003).
[23] M. Le Van Quyen, J. Martinerie, C. Adam, and F. J. Varela, Phys. Rev. E **56**, 3401 (1997).
[24] P. A. Robinson, P. M. Drysdale, H. Van der Merwe, E. Kyriakou, M. K. Rigozzi, B. Germanoska, and C. J. Rennie, Neuroimage **31**, 585 (2006).